Journal of Materials Chemistry B

ROYAL SOCIETY OF CHEMISTRY

PAPER

View Article Online
View Journal | View Issue

Cite this: *J. Mater. Chem. B*, 2025, **13**, 11001

Intercalating cerium into layered double hydroxide as a promising reactive oxygen species scavenger for inflammation treatment

Thanh-Truc Nguyen, [a] Gábor Varga, [ad] Jessica Pickett,[b] Miaomiao Wu,[a] Hang Thu Ta, *[b] Zhi Ping Xu*[ac] and Run Zhang *[a]

Received 9th April 2025,
Accepted 7th August 2025

DOI: 10.1039/d5tb00829h

rsc.li/materials-b

Nanoceria has been studies for many decades given its capability in quenching reactive oxygen species (ROS) in inflammatory diseases. The regenerative exchanges between Ce^{3+} and Ce^{4+} as well as the ratio between these two cations have been reported as one of the most important factors for enhancing their ROS scavenging activity. In this study, a novel method for increasing the active sites and the ratio of Ce^{3+}/Ce^{4+} utilising layered double hydroxides (LDH) nano system has been developed. Ce doped LDH nanoparticles with various Ce-loading amounts were prepared, and the physicochemical properties were characterised. The anti-hydrogen peroxide (H_2O_2) capability of these Ce–LDH NPs has been evaluated *in vitro* against the treated RAW 264.7 macrophages. The optimal Ce–LDH NPs were then introduced into a 3D cell-hydrogel construct resembling the pathological morphology of atherosclerosis to investigate their ability to capture ROS in a more complex cell system. The successful development of this Ce-doped LDH nanosystem provides a promising biocompatible agent for future treatment of inflammatory disorders.

Introduction

The human body must depend on its inflammatory process to fight against various causes of infection such as viruses, bacteria, reactive oxygen species (ROS), and toxins.[1–3] However, our innate immune system may not suffice; hence, a vast number of diseases have been emerged from the inflammation.[4] Amongst multiple factors in the progression of inflammatory diseases, the production of ROS has been reported as one of the key aspects of pathophysiological mechanisms.[5,6] Normally, a proper amount of ROS generated by phagocytic cells is capable to scavenge pathogens and useful for the human body; however, when ROS become excessive, oxidative stress happens and can cause tissue dysfunction, which leads to uncontrolled inflammatory responses and paves a way for many detrimental diseases such as neurodegenerative diseases, cardiovascular diseases, bowel disease, rheumatoid arthritis, and lately, the cytokine storm observed in COVID-19 patients.[5,7–10]

In their radical or molecular forms, ROS contain three primary species: the superoxide anion ($O_2^{\bullet-}$), hydrogen peroxide (H_2O_2), and the hydroxyl radical ($^{\bullet}OH$). $O_2^{\bullet-}$ and $^{\bullet}OH$ are usually referred to as "free radicals" whilst H_2O_2 plays as a non-radical ROS, which is produced through the process of oxidative folding.[11] Although the pathogenesis of inflammatory diseases is complicated, targeting excessive ROS has been perceived as a crucial approach in the design of therapeutics for many decades, starting with natural antioxidative compounds extracted from herbal sources such as polyphenols, vitamins, and carotenoids to inorganic materials.[12–16] Recently, thanks to the development of nanotechnology, these antioxidants have been undergoing synthetic processes to overcome the common drawbacks of their tendency to degrade, poor adsorption, and non-specific distribution.[17–21]

One of the promising candidates among the inorganic antioxidants in nanomedicines is cerium oxide nanoparticles (CeO_2 NPs).[22,23] In its oxide state, cerium (Ce) possesses two valent states on the oxide surface, including trivalent (Ce^{3+}) and tetravalent (Ce^{4+}). Interestingly, these two valences continuously convert from one oxidation state to the other, and in doing so, the conversion mimics both the superoxide dismutase (SOD) and catalase effects.[24–26] If there are excessive superoxide radicals, Ce^{3+} would react with them to form Ce^{4+} and release H_2O_2, then Ce^{4+} continues to quench H_2O_2 and converts itself back into Ce^{3+}. This self-regenerating cycle of redox reactions leads to the ultimate elimination of ROS.[23,27,28]

[a] *Australian Institute for Bioengineering and Nanotechnology, The University of Queensland, St Lucia, Queensland, 4072, Australia. E-mail: r.zhang@uq.edu.au, gordonxu@uq.edu.au*
[b] *School of Environment and Science, Griffith University, Nathan, Queensland, 4111, Australia. E-mail: h.ta@griffith.edu.au*
[c] *Institute of Biomedical Health Technology and Engineering and Institute of Systems and Physical Biology, Shenzhen Bay Laboratory, Shenzhen, 518107, China*
[d] *Interdisciplinary Excellence Centre, Department of Applied and Environmental Chemistry, University of Szeged, Rerrich Béla tér 1, Szeged, H-6720, Hungary*

Many studies have focused on this interesting dynamic and concluded that nanoceria with the higher molar ratio of Ce^{3+}/Ce^{4+} could better perform its imitation of SOD.[24,25,29–31] Several synthetic methods have also been investigated to increase the molar ratio of Ce^{3+}/Ce^{4+} and ultimately to enhance the antioxidant capabiltiy.[24]

Amongst novel nanocarriers, layered double hydroxides (LDHs), a type of two dimensional (2D) layered nanomaterials, have gained a significant attention regarding their versatility in modifying the charged hydroxide layers and loading drugs, resulting in a final product that could be used as a therapeutic agent in biomedical applications.[32–36] This is primary because of intrinsic properties of LDH nanoparticles, including high biocompatibility, high drug loading capability, positively charged surface with capability of biofunctionalization, *etc.* More importantly, LDH can be easily synthesized, allowing for large scale preparation for future translational studies. The structure of LDHs is described as brucite-like similar to that of $Mg(OH)_2$. In this structure, the octahedral coordination of divalent cations by six hydroxyl groups is partially replaced by trivalent cations, resulting in positive charges in the sheet. The net positive charge is compensated by anions in the interlayer region. The formula of LDHs is described as $[M^{2+}_{1-x}M^{3+}_{x}(OH)_2]^{x+}(A^{n-})_{x/n}{\cdot}mH_2O$, where M^{2+} and M^{3+} are divalent and trivalent cations, respectively; the value of x is equal to the molar ratio of $M^{3+}/(M^{2+} + M^{3+})$ ranging from 0.2 to 0.4, whereas A^{n-} is the interlayer anion. Typically, LDHs could be found in the pristine formula of $Mg_6Al_2(OH)_{16}CO_3{\cdot}4H_2O$ or $Mg_6Al_2(OH)_{16}Cl{\cdot}4H_2O$.[37] Notably, both Mg^{2+} and Al^{3+} could be replaced by other metal cations that possess the desired function in terms of biomedical applications.[37–44]

Utilising the flexibility of LDHs mentioned above, in this study, Ce^{3+} was introduced into LDHs lattice by replacing various percentages of Al^{3+} with the goal of enhancing the anti-ROS ability of the conventional nanoceria (Scheme 1A and Fig. S1). In our hypothesis, intercalating Ce into the LDH layers could increase the active surface of this metal ion compared with convention sole Ce metal-based nanoparticle (*e.g.*, CeO_2). These Ce-doped LDHs were then stabilised with bovine serum albumin (BSA) to prevent the prospective aggregations of nanoparticles in the physiological environment, benefiting their cellular uptake and reducing inflammatory responses.[45] Furthermore, the synthesised Ce–LDH NPs were labelled with fluorescein isothiocyanate (FITC) to track their cellular internalisation capabilities (Fig. S2).[46] Macrophages RAW 264.7 were used as a main cell line in *in vitro* assays, and a more complex cell system named three-dimensional (3D) cell-hydrogel structure combining smooth muscle cells, endothelial cells, and macrophages was used to evaluate the efficacy of these NPs as promising ROS scavengers for the treatment of inflammatory diseases (Scheme 1B).

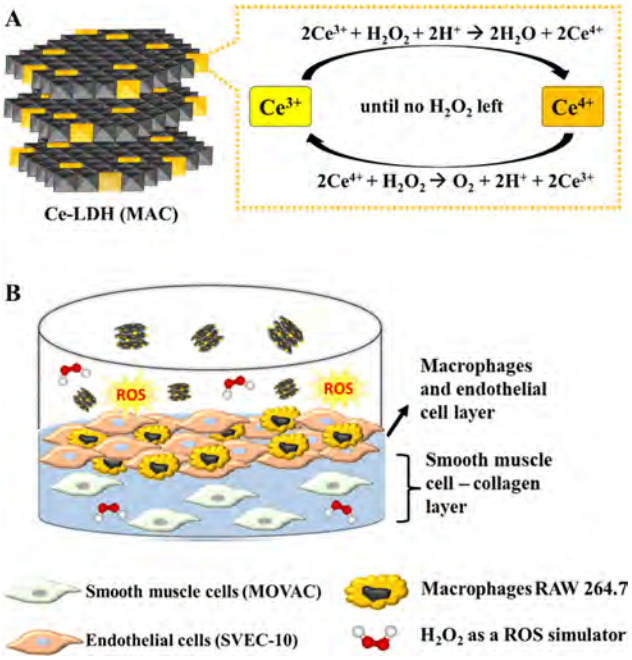

Scheme 1 Development of the Ce incorporated LDH nanoparticles (MAC) for ROS scavenging for inflammation treatment. (A) The MAC nanoparticles and the mechanism for Ce-mediated ROS scavenging. (B) Demonstrating the application of MAC0.05 for ROS scavenging in 3D cell-hydrogel structures.

Experimental

Materials

Magnesium chloride hexahydrate ($MgCl_2{\cdot}6H_2O$), aluminium chloride hexahydrate ($AlCl_3{\cdot}6H_2O$), cerium(III) chloride heptahydrate ($CeCl_3{\cdot}7H_2O$), sodium hydroxide (NaOH), hydrochloric acid (HCl), ethanol absolute 98%, hydrogen peroxide 30% (H_2O_2), neocuproine, copper(II) sulfate ($CuSO_4$), bovine serum albumin (BSA), phosphate-buffered saline (PBS 10×), fluorescein isothiocyanate (FITC), and 2′,7′-dichlorodihydrofluorescein diacetate (DCFH-DA) were purchased from Sigma-Aldrich. Macrophage RAW 264.7, lung cancer cell line A549, MOVAS, and SVEC4-10 were purchased from American type culture collection (ATCC, Manassas, VA). Dulbecco's modified Eagles medium (DMEM) high glucose, fetal bovine serum (FBS), penicillin–streptomycin (PS), MTT (3-(4,5-dimethylthiazol-2-yl)-2,5-diphenyltetrazolium bromide) were obtained from Invitrogen, Australia. Milli-Q water was used in all experiments.

Physicochemical characteristics of MAC

Size distributions and zeta potentials of LDH NPs were measured using a Zetasizer analyzer (Malvern). The morphology and size of nanoparticles were checked by transmission electron microscopy (TEM, Hitachi HT-7700). The elemental mapping and EDS spectra were measured using Hitachi HF5000. The chemical bonds and composites in samples were examined using Fourier transform infrared (FTIR, Nicolet iS10 spectrometer) spectroscopy and X-ray diffraction (XRD) on a powder X-ray diffractometer (Bruker) with Cu Kα radiation (λ = 0.15418 nm) at a scanning rate of 2 deg min^{-1} from 2θ = 5° to 70°. The ICP (Inductively Coupled Plasma) Spectroscopy was used to measure and identify elements within the MAC samples matrix. The X-ray photoelectron spectroscopy (XPS) of LDH NPs was taken using

Kratos AXIS Supra Plus XPS system which uses a dual monochromate Al Kα/Ag Lα X-ray source.

Determination the percentage of Ce(III) in whole LDH NPs using the spectrofluorometer

The calibration curve of different concentrations of Ce(III) was established as follows: 0.001 mol of $CeCl_3{\cdot}7H_2O$ was dissolved in 60 mL of DI water containing 1 mL of 32% HCl. This solution was shaken for 30 min and then diluted into different concentrations with Milli-Q water. After that, the emission spectra of these solutions were measured by the fluorescence spectrofluorometer (Hitachi F 4501, Japan) using excitation and emission at 255 and 355 nm, respectively.

For the MAC samples with different percentages of Ce, 2 mL of each sample was added with 200 μL of 32% HCl. The mixture was left for at least 1 day to completely dissolve the MAC NPs. These solutions were then diluted to measure the emission intensity by fluorescence spectrofluorometer (Hitachi F 4501, Japan) with excitation and emission at 255 and 355 nm, respectively.

Anti-H_2O_2 capability of MAC in 1× PBS

The CUPRAC method was used to determine the anti-H_2O_2 capability of MAC in 1× PBS.[47] Basically, the chromogenic oxidizing reagent of the CUPRAC method (bis(neocuproine) copper(II) chloride (Cu(II)–Nc)) reacts with *n*-electron-reductant antioxidants (AOX) as follows:

$$n\mathrm{Cu(Nc)_2}^{2+} + n\text{-electron reductant (AOX)} \leftrightarrow n\mathrm{Cu(Nc)}^{2+} + n\text{-electron oxidized product} + n\mathrm{H}^{+}$$

where Cu(II)–Nc has a specifical absorbance at 450 nm. In this project, the remaining H_2O_2 after reacting with various MAC samples interacted with the mixture of copper sulfate and neocuproine to produce the bis(neocuproine)copper(II) chloride.

Briefly, MAC samples at the same concentration of Ce of 25 μg mL^{-1} were added into 0.4 mM of H_2O_2 solution. The mixture was incubated at room temperature for 30 min. Then, 500 μL of $CuSO_4$ 10 mM and 500 μL of neocuproine 10 mM were added to the mixture. After incubation for 30 min at room temperature, the absorbances of samples were measured by a Shimadzu UV-vis spectrometer at 450 nm. The standard curve was established at every repeated test by adding 500 μL of 1× PBS, 500 μL of $CuSO_4$ 0.01 M, 500 μL of neocuproine 0.01 M, and 500 μL of different concentrations of H_2O_2 (from 0–0.5 mM). The absorbance of the sample without MAC was regarded as 0% H_2O_2 reduction.

In vitro ROS scavenging of MAC0.05

Macrophage RAW 264.7 and fibroblast NIH/3T3 cells were seeded into a 24-well plate at a density of 25 000 cells per well. After 24 h incubation, the cells were separately treated with different concentrations of MA@BSA at the concentration of 4 μg mL^{-1} and MAC0.05@BSA at different concentrations of 4, 8, and 20 μg mL^{-1}. After an additional 2 h incubation, the macrophages were stimulated with 1.5 mM H_2O_2 for 30 min in an incubator at 37 °C and 5% CO_2. Intracellular ROS levels were detected by incubating the cells with 12 μg mL^{-1} DCFH-DA for 30 min in an incubator at 37 °C and 5% CO_2. Then all the media was removed, and 1 mL of 1× PBS was added to collect the cell suspension into tubes for flow cytometry ($\lambda_{ex/em}$ = 485/530 nm).

Hemolysis assay of MAC0.05@BSA

Fresh blood (1 mL) was centrifuged at 1000 rpm for 15 min (acceleration and brake set at 4) to separate plasma with red blood cells (RBCs). The RBCs were obtained by separating the plasma followed by washing the RBCs twice with PBS of pH 7.4 at 1000 rpm (~110 g) for 15 min. A stock of RBCs was created by diluting washed RBCs with PBS at pH 7.4 with a ratio of RBCs : PBS = 1 : 50. Then, the MAC0.05@BSA samples at different concentrations (4, 8, 20, and 40 μg mL^{-1}) were mixed with that stock RBCs with the ratio of MAC : RBCs solution = 1 : 9.1% Triton-X 100 and PBS at pH 7.4 were used as positive and negative control, respectively. The Eppendorf tubes were then placed in an incubator at 37 °C for 2 h. After incubation, the tubes were centrifuged at 14 000 g in 20 min and the supernatant was transferred to a 96-well plate for measuring absorbance at 545 nm. Percentage of hemolysis was calculated using the equation below:

$$\text{Hemolysis (\%)} = \frac{\text{OD sample} - \text{OD negative control}}{\text{OD positive control} - \text{OD negative control}} \times 100$$

Formation of cell-hydrogel constructs for testing cellular uptake and ROS scavenging

Collagen hydrogel was prepared from Cultrex® 3D Culture Matrix Rat Collagen I according to the manufacturer protocol. All reagents were pre-cooled on ice for 30 min to prevent any premature gelation upon mixing. Collagen was diluted to 2 mg mL^{-1} in 10× DMEM and buffered to pH 7 with 1 N NaOH. MOVAS cell suspension was mixed homogenously within the hydrogel solution and added up to the desired volume with DI water for a final concentration of 1.0×10^5 cells per mL. 50 μL gel per well was added to a 96-well plate and left to set in the cell incubator at 37 °C for 1 h. After gel solidification, 100 μL of 2.0×10^5 cells per mL SVEC4-10 suspension was introduced to the cell-hydrogel constructs for endothelialisation. The constructs were cultured for 5 days with high-glucose DMEM to allow sufficient time for a confluent endothelial monolayer to be formed. Media was refreshed every 24 h to maintain the overall viability of the cell-hydrogel constructs. Then, the final layer of RAW 264.7 was seeded with a concentration of 1.0×10^5 cells per mL, incubated for 24 h.

For testing cellular uptake, the cell culture media was replaced with the new media containing MA-FITC@BSA and MAC0.05-FITC@BSA (at the concentration of whole LDH = 4 μg mL^{-1}). After 1 h of incubation, the media were removed, then PBS 1× was added to each well. The fluorescence intensity of each well was recorded by a plate reader ($\lambda_{ex/em}$ = 485/530 nm). For evaluating the ROS scavenging, the media was replaced with the new media containing MA@BSA and

MAC0.05@BSA (at the concentration of whole LDH = 4 μg mL^{-1}). After 2 h of incubation, the media was replaced with 1.5 mM H_2O_2 for 30 min in an incubator at 37 °C and 5% CO_2. Intracellular ROS levels were detected by incubating the cells with 12 μg mL^{-1} DCFH-DA for 30 min in an incubator at 37 °C and 5% CO_2. Then all the media were removed, and 100 μL of PBS 1× was added to collect the cell suspension into tubes. The 96-well plate was taken to read the FI at Ex/Em = 485/530 nm by a plate reader.

Results and discussion

Physicochemical characterisation of MAC samples

Fig. 1A shows that the size of MAC increased from 146 to 335 nm with the ascending amount of Ce doped in LDH from 0.025 to 0.2. The data of MAC0.025, MAC0.05, and MAC0.1 were not much different in their size whilst MAC0.05 had the smallest polydispersity index (PDI) among MAC samples (Fig. 1A). The zeta potentials of all samples were from 25 to 35 mV. Fig. 1B shows the estimated formula for all MAC nanoparticles based on the ICP data, and clearly the Ce loading efficiency in the synthetic process was in the range of 84–87%. As a result, the designed chemical formula of MAC was quite similar to the calculation from the ICP data.

Similar to that of LDH nanoparticles, FIIR spectra of MAC samples show the peak at 1360 cm^{-1} and 3460 cm^{-1} for all samples (Fig. S3). The peak at 1360 cm^{-1} was attributed to the carbonate formation in LDH nanoparticles, while the peak at 3460 cm^{-1} represented the O–H in the hydroxide layer and H_2O. During the MAC preparation, CO_2 reacts with OH^- to form CO_3^{2-}, which is then intercalated or adsorbed on the surface of LDH particles.[48]

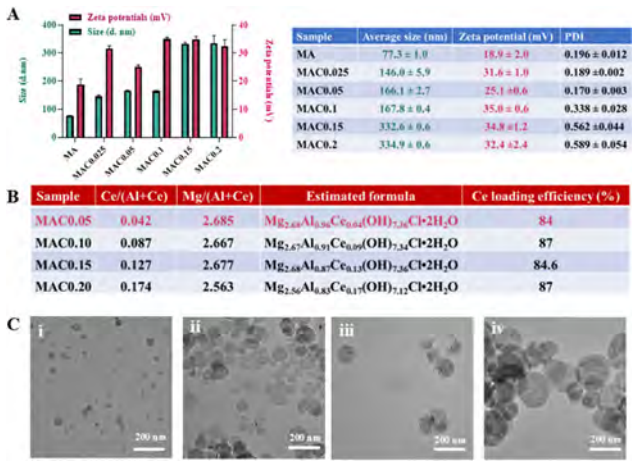

Sample	Average size (nm)	Zeta potential (mV)	PDI
MA	77.3 ± 1.0	18.9 ± 2.0	0.196 ± 0.012
MAC0.025	146.0 ± 5.9	31.6 ± 1.0	0.189 ±0.002
MAC0.05	166.1 ± 2.7	25.1 ±0.6	0.170 ± 0.003
MAC0.1	167.8 ± 0.4	35.0 ± 0.6	0.338 ± 0.028
MAC0.15	332.6 ± 0.6	34.8 ±1.2	0.562 ±0.044
MAC0.2	334.9 ± 0.6	32.4 ±2.4	0.589 ± 0.054

B

Sample	Ce/(Al+Ce)	Mg/(Al+Ce)	Estimated formula	Ce loading efficiency (%)
MAC0.05	0.042	2.685	$Mg_{2.68}Al_{0.96}Ce_{0.04}(OH)_{7.36}Cl{\cdot}2H_2O$	84
MAC0.10	0.087	2.667	$Mg_{2.67}Al_{0.91}Ce_{0.09}(OH)_{7.34}Cl{\cdot}2H_2O$	87
MAC0.15	0.127	2.677	$Mg_{2.68}Al_{0.87}Ce_{0.13}(OH)_{7.36}Cl{\cdot}2H_2O$	84.6
MAC0.20	0.174	2.563	$Mg_{2.56}Al_{0.83}Ce_{0.17}(OH)_{7.12}Cl{\cdot}2H_2O$	87

Fig. 1 Physicochemical properties of MAC samples. (A) The size distributions and zeta potentials, and PDI of MA, MAC0.025, MAC0.05, MAC0.1, MAC0.15, and MAC0.2. (B) The calculated chemical formula of MAC based on ICP results. (C) The TEM images of (i) MA-RT, (ii) MAC0.05-RT, (iii) MAC0.05-100-4 h, and (iv) MAC0.05-100-24 h. RT means room temperature, and 100 means the LDH NPs prepared by hydrothermal treatment at 100 °C with corresponding time spans.

As shown in Fig. 1C, the TEM images of all LDH–Ce NPs (MAC0.05) subjected to various treatment are in hexagonal shapes, which is similar to the original MA LDH NPs. The preparation at room temperature resulted in the smallest MAC0.05 in size (166.1 ± 2.7 nm) compared with those treated at 100 °C for 4 and 24 h. The longer the hydrothermal treatment time for LDH NPs, the larger in the size of prepared NPs. However, when the hydrothermal treatment was longer, there were several clusters formed, which resulted in a bigger size value.

As shown in Fig. S4, the structural characterization and phase identification of Ce–LDH NPs were studied with X-ray diffraction (XRD). In all LDH samples, the high-intensity peaks were observed at 11.17°, 22.1–22.43°, 34.29–34.46°, 38.19–38.62°, and 60.0–62.09° respective to the (003), (006), (012), (011), and (110) crystal planes. Based on Bragg's law, the reflections with an interlayer spacing (d_{003}, d_{006}, d_{012}, d_{011}, and d_{110}) were around 0.792, 0.396, 0.261, 0.234, and 0.151 nm, respectively. These data were consistent with previously reported lattice parameters of LDH.[15,18] The thickness of the layer was estimated to be around 11.4 nm along the (003) plane.[26,35,48,49] However, when introducing Ce into the LDH nanosheets, the LDH nanoparticles showed the polycrystalline nature and cerium oxides were expected to form on the surface of LDH, which showed a broad peak at 28–29°, corresponding to the (111) plane of CeO_2.[50] Higher peak of (111) was observed for MAC samples with larger amount of Ce loading, suggesting that more CeO_2 phase was formed.

Fig. S5 shows the XPS spectra of MAC0.05, MAC0.1, MAC0.15, and MAC0.2. The ratio between Ce^{3+}/Ce^{4+} in each sample was determined by the relative intensity of each peak of Ce^{3+} compared to Ce^{4+}. For all samples, there were two significant peaks at the binding energy of 881–882 eV and around 900 eV, which are assigned to Ce^{3+}'s binding energy. Other peaks (888, 902, and 908 eV) belonged to binding energy of Ce^{4+}.[51,52] The Ce^{3+}/Ce^{4+} ratio on the surface of MAC0.05, MAC0.1, MAC0.15, and MAC0.2 was calculated as follows, 31.5%/69.5%, 40%/60%, 42%/58%, and 45%/55%, respectively. The percentages of Ce^{3+} increased with the loading amount of Ce^{3+}, and MAC0.2 had the greatest percentage of Ce^{3+} on the active surface of all MAC nanoparticles. Successful Ce intercalation was further confirmed by the elemental mapping and EDS spectra of MAC0.05. As shown in Fig. S6, despite low concentration of Ce, its intercalation in LDH nanoparticles was observed and the EDS spectrum showed Ce's loading at positions of energy from 5–6 keV.

The percentage of Ce^{3+} in all MAC nanoparticles was also determined by fluorescence method, where the Ce^{3+} has intense emission at 355 nm with excitation at 255 nm whilst Ce^{4+} does not show its peaks at this wavelength.[53] The standard curve for Ce^{3+} detection was determined by fluorescence analysis (Fig. S7). As shown in Fig. 2A, the emission of MACs was tested and MAC0.1 showed highest emission intensity in all MAC nanoparticles. The Ce^{3+} was calculated using the standard curve in Fig. S7A, and the Ce^{3+}'s percentage to the whole bulk MAC nanoparticles were then determined by dividing the

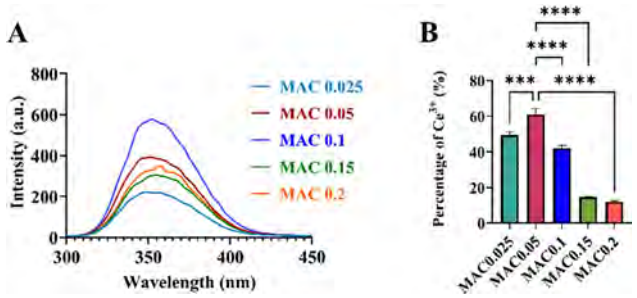

Fig. 2 Determination of the Ce^{3+} percentage in the bulk LDH using fluorometric method. (A) Fluorescence spectra of MAC nanoparticles with excitation at 255 nm. (B) The percentage of Ce^{3+} in the whole MAC (data represent mean ± SD). *** indicates P = 0.001, **** indicates $P < 0.0001$.

concentration of Ce^{3+} to the bulk MAC nanoparticles. As shown in Fig. S7B, the low loading amount of Ce^{3+} resulted in a high percentage of Ce^{3+} in general, and MAC0.05 had the highest Ce^{3+} percent among 5 samples (61% of Ce^{3+}). This ratio was much higher than that on the surface of MAC0.05 determined by XPS (31.5%), indicating that on the surface, Ce^{3+} were mostly oxidised to Ce^{4+}. In general, the XPS results demonstrated the ratio of Ce^{3+}/Ce^{4+} only on the active surface, whilst this fluorometric method is able to reveal the real percentage of Ce^{3+} in a whole LDH nanosystem.[53] This result showed that MAC0.05 was the optimal Ce–LDH NPs that had the highest ratio of Ce^{3+}/Ce^{4+}.

ROS scavenging capability of MAC in PBS

We then evaluated the ROS scavenging capability of MAC by measuring their anti-H_2O_2 performance in PBS. As shown in Fig. 3A, MAC0.025, MAC0.1, MAC0.15, and MAC0.2 had lower capability to reduce H_2O_2 compared to that of MAC0.05, confirming that MAC0.05 had the optimal amount of Ce loaded in LDH for ROS scavenging in PBS. The MA without Ce(III) loading also exhibited ROS scavenging capability with a 15% H_2O_2 reduction. Compared to the MAC0.05 sample, with a lower concentration of Ce at 25 μg mL^{-1}, the NPs quenched up to 64.8% of 0.4 mM H_2O_2. Moreover, the percentage of H_2O_2 being quenched by MAC0.05 was about 1.1–1.6 times higher than that of CeO_2 NPs at different incubation times using the same Ce concentration (Fig. 3B). The quenching of H_2O_2 by Ce^{3+}/Ce^{4+} is because of the specific oxidation/reduction showing in Scheme 1A. More importantly, although both MAC0.05 and CeO_2 demonstrated similar overall H_2O_2 quenching capacity after extended treatment time (>6 hours), MAC0.05 achieved significantly faster quenching kinetics. This rapid response suggests the potential of MAC0.05 for applications requiring prompt ROS modulation, such as acute oxidative stress treatment or inflammation management.

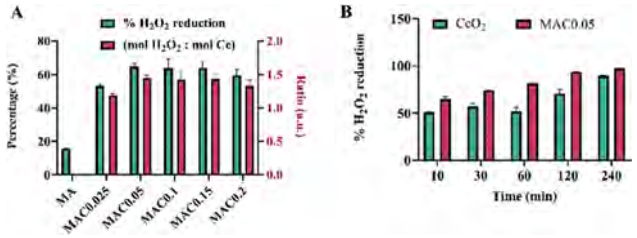

Fig. 3 The ROS scavenging capabilities of CeO_2, MA, and MAC in PBS. (A) The anti-H_2O_2 capability of synthesised LDH including MA, MAC0.025, MAC0.05, MAC0.1, MAC0.15, and MAC0.2. (B) The comparison of anti-H_2O_2 capability between CeO_2 and MAC0.05. The concentration of Ce in all samples was kept at 25 μg mL^{-1} theoretically.

The high H_2O_2 scavenging performance of MAC could thus be attributed to the increased active sites of Ce in this LDH nano system. Of various MA and MAC nanoparticles, MAC0.05 exhibited highest percentage of H_2O_2 scavenging as well as highest ratio (H_2O_2 : Ce). As of the XPS (Fig. S5) and the fluorometric data (Fig. 2), MAC0.05 has the highest ratio of Ce^{3+}/Ce^{4+}. These results suggest that the Ce^{3+} in the bulk of MAC also contributed significantly to enhancing H_2O_2 quenching ability. As a result, MAC0.05 was selected as the optimal nanoparticle for further studies of ROS scavenging in biological system.

To further validate the performance of MAC0.05 in ROS scavenging, hydroxyl radical ($^{\bullet}OH$)-responsive fluorescence probe was applied to determine the changes in fluorescence spectra of the Fenton reaction system with and without MAC0.05 treatment. MAC0.05 in solution containing H_2O_2 was added with CCA, a small molecule-based fluorescence probe for $^{\bullet}OH$ detection.[54] As shown in Fig. S8, control groups, including MAC, MAC + H_2O_2, and MAC + CCA, MAC + CCA + Fe^{2+} showed negligible emission. Without MAC0.05 treatment (CCA + H_2O_2 + Fe^{2+}), the mixture of CCA with $^{\bullet}OH$ (Fe^{2+} + H_2O_2 Fenton reaction system) showed intense emission, which is attributed to the conversion of non-fluorescent CCA to fluorescent 7OH-CCA through an $^{\bullet}OH$-mediated specific hydroxylation reaction. Small increase in CCA's fluorescence was observed for the MAC0.05 solution containing H_2O_2 (MAC + H_2O_2 + CCA), which could be attributed to the Ce^{3+}-involved Fenton reaction and the production of $^{\bullet}OH$ as one of intermediates (reaction (1)). The produced $^{\bullet}OH$ quickly reacts with H_2O_2 to form HO_2^- (reaction (2)), which is followed by quenching reaction with Ce^{4+} (reaction (3)) through the cascade reactions below:

$$Ce^{3+} + H_2O_2 + H^+ \rightarrow Ce^{4+} + {}^{\bullet}OH + H_2O \quad (1)$$

$$^{\bullet}OH + H_2O_2 \rightarrow HO_2^- + H_2O \quad (2)$$

$$HO_2^- + Ce^{4+} \rightarrow O_2 + Ce^{3+} + H^+ \quad (3)$$

Subsequently $^{\bullet}OH$ quenching by MAC0.05 was also validated by fluorescence measurement of the Fenton reaction solution treated with MAC0.05 (MAC + H_2O_2 + CCA + Fe^{2+}). Small increase of the emission was noticed in comparison with MAC + H_2O_2 + CCA group, while the emission intensity was significantly (approximately 2-times) lower than the one without treatment. The results demonstrate that MAC0.05 is a potent scavenger for $^{\bullet}OH$.

Biofunctionalization of MAC0.05

To enhance the colloidal stability and biocompatibility, different concentrations of MAC0.05 (1.0, 0.5 and 0.1 mg mL^{-1}) were

coated with BSA according to a ratio of BSA : MAC0.05 = 5 : 1.[55] As shown in Fig. 4A, no remarkable differences were observed among the three MAC0.05 concentrations. The dynamic sizes of the MAC0.05@BSA are variable from 160 to 190 nm after coating with BSA. The PDI of all samples is below 0.3, implying proper dispersion of all nanoparticles after BSA coating. Furthermore, the zeta potential of LDH was changed to be negative after coating with BSA (from 38 mV to −15.6 mV) further confirming the successful BSA coating on MAC0.05. Colloidal stability of MAC0.05@BSA was then investigated in water, PBS buffer, and cell culture medium (Fig. 4B). The dynamic size of MAC0.05@BSA in these three media was about 150–160 nm (Fig. 4A), and no significant changes of size distribution were observed over the incubation times of 0 h, 24 h, and 48 h (Fig. 4B), demonstrating high colloidal stability of the MAC0.05@BSA.

The biocompatibility of MAC0.05@BSA NPs was evaluated based on their effect on the viability of two cell lines, including lung cancer cell line A549 and macrophage RAW264.7. Fig. 4C shows the percentage of cell viability after being treated with different concentrations of MAC0.05@BSA (0, 4, 8, 20, and 40 μg mL^{-1}). The overall trend showed the adhesive A549 tolerated MA@BSA and MAC0.05@BSA better than RAW 264.7. This phenomenon was also reported by Liu *et al.*, in which the nanocomposites containing Ce expressed toxicity to macrophages much higher than the cancer cell line, although a different kind of cancer cell was used in their study.[56] Additionally, when the concentrations of LDH NPs were increased from 20 to 40 μg mL^{-1}, there was a significant decrease in viability of both cell lines. The effect on the cell viability of MAC0.05@BSA to fibroblast NIH/3T3 was also tested by MTT assay. As shown in Fig. S9A, in comparison with the control group (untreated NIH/3T3 cells), negligible changes in the cell viability were observed after the treatment of NIH/3T3 with MAC0.05@BSA (0, 4, 8, 20, and 40 μg mL^{-1}). After 24 h incubation of NIH/3T3 cells with 40 μg mL^{-1} MAC0.05@BSA, the cell viability was greater than 82%, indicating the high biocompatibility of MAC0.05@BSA.

The biocompatibility of MAC0.05@BSA NPs was then evaluated by testing their hemolytic activity against red blood cells (RBCs). As shown in Fig. 4D, similar to negative control group of PBS pH 7.4, nearly no hemolysis of RBCs was observed after incubation with MA@BSA at the concentration of 4 μg mL^{-1} and MAC0.05@BSA at the concentrations of 4, 8, 20, and 40 μg mL^{-1} after 2 h. In sharp contrast, RBCs treated with 1% Triton-X 100 (positive control group) showed remarkable hemolysis. In our previous study, good hemocompatibility of CeO_2 NPs loaded in chitosan nano-cocktails was reported.[24] These data showed that cerium loaded within LDH nanocarrier (MAC0.05@BSA) is also safe to human blood at a concentration of 40 μg mL^{-1}.

ROS scavenging capability of MAC0.05@BSA in cells and 3D cell constructs

Prior to the *in vitro* evaluation of ROS scavenging capability, cellular uptake of MAC0.05@BSA into RAW2644.7 was investigated using FITC labelled nanoparticles (MAC0.05-FITC@BSA NPs). As shown in Fig. S10, there was no difference in the cellular uptake at both the low and high concentrations of the NPs. The mean fluorescence intensity (MFI) of cells treated with MAC0.05-FITC@BSA NPs increased during the incubation time from 1 to 4 h, while it decreased significantly after 8 h

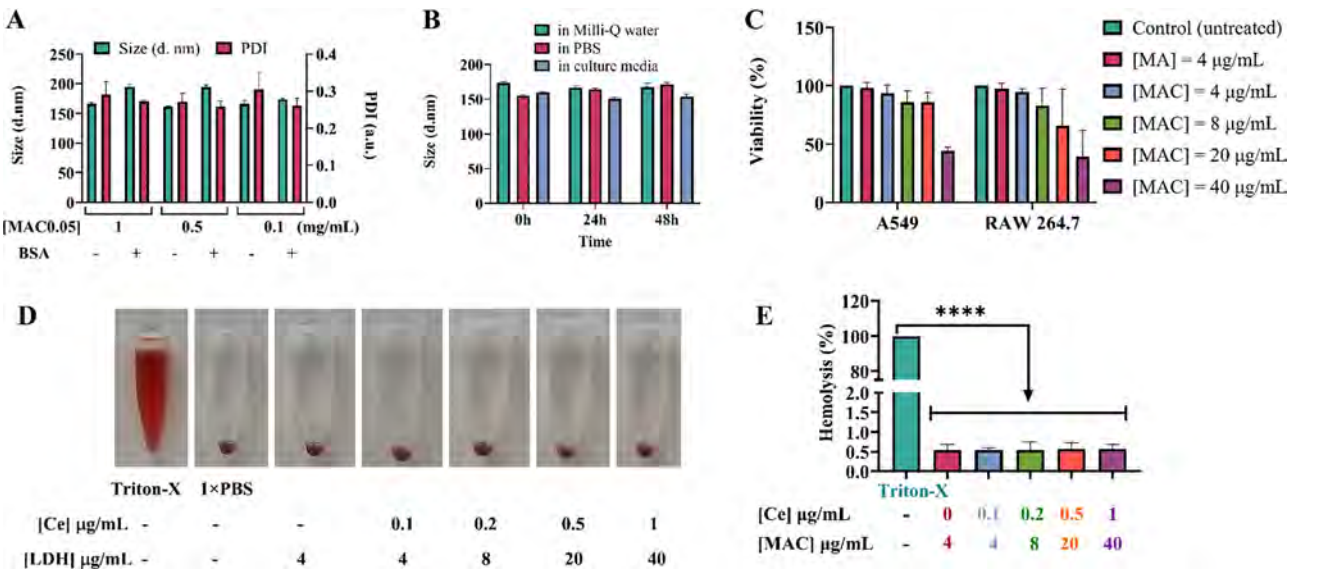

Fig. 4 The size distributions, colloidal stabilities of MAC0.05@BSA, and the biocompatibility of MA@BSA and MAC0.05@BSA based on MTT assay and haemolytic assay. (A) The size distributions and PDI of MAC0.05@BSA using different concentrations of MAC0.05 with and without BSA coating. (B) The colloidal stability of MAC0.05@BSA with the final concentration of LDH at 500 μg mL^{-1}. (C) The viability of MA@BSA (4 μg mL^{-1}) and MAC0.05@BSA at different concentrations (4, 8, 20, and 40 μg mL^{-1}) to A549 and RAW564.7 cells. (D) Photographs of RBCs samples and treated with Triton-X 100, PBS, MA@BSA (4 μg mL^{-1}) and MAC0.05@BSA (4, 8, 20, and 40 μg mL^{-1}). (E) Haemolytic activity of MA@BSA with the concentration of 4 μg mL^{-1} and MAC0.05@BSA with different concentrations of 4, 8, 20, and 40 μg mL^{-1} after treated with RBCs after 2 h. Triton-X 100 1% and PBS pH 7.4 were used as positive and negative control, respectively.

incubation. After 4 h, FITC in the NPs would be released into the culture media and lost its fluorescence due to prolonged incubation times.

One of the most important aspects about MAC NPs is their effectiveness in scavenging ROS, as shown in Fig. 5 for MA@BSA and MAC0.05@BSA in a monolayered cell model. As shown in Fig. 5A, fluorescence imaging of stimulated cells showed intense green fluorescence, which is derived from the reaction of DCFH-DA with ROS. Treatment with MA@BSA slightly decreased the green emission, while in sharp contrast, no green emission was observed for the cells treated with MAC0.05@BSA, indicating the successful elimination of ROS by the treatment. In all cases, Ce–LDH NPs at 4 μg mL^{-1} exhibited good anti-ROS capability (Fig. 5B). There was a fluctuation in the percentage of ROS remaining in macrophages RAW 264.7 after being treated with MA@BSA. Similar percentages of ROS remaining in macrophages after treating cells within 2 h, while ROS levels increased at 4 h, attributable to the oxidation of MA@BSA. For the cells treated with MAC0.05@BSA, the ROS level increased after 4 h treatment, with the minimal ROS at 2 h treatment. This observation could suggest the optimal treatment time should be 2 h. Overall, the optimal concentration of MAC0.05 against ROS was 4 μg mL^{-1}, which means that the concentration of Ce in this sample was at a low dose of 0.1 μg mL^{-1}. In this case, the NPs quenched up to 80% ROS inside the macrophages that were stimulated with 1.5 mM of H_2O_2. In a previous study, Wu *et al.* reported that using 0.1 mM of H_2O_2 to stimulate ROS and treating macrophages with iron oxide–CeO_2 core shell NPs in 1 h with the concentration of Ce of 11.2 μg mL^{-1} could scavenge 50% of ROS.[25] Clearly, the anti-ROS capability of MAC0.05@BSA was 112-times higher than Ce incorporated in NPs (CeO_2) using the method in previous research.[18] These data suggested that the new Ce–LDH NPs had promising effectiveness in quenching excessive ROS at lower doses of Ce.

The ROS quenching efficacy of the MAC0.05@BSA nanoparticles was also investigated in NIH/3T3 cells. H_2O_2-stimulated NIH/3T3 cells were treated with MAC0.05@BSA (0, 4, 8, and 20 μg mL^{-1}) for 1–4 h, and the percentage of remaining ROS was measured. As shown in Figure Fig. S9B, increasing MAC0.05@BSA's concentration and treatment time leads to the enhanced ROS quenching. At the concentration of 20 μg mL^{-1} of MAC0.05@BSA, greater than 30% of ROS quenching was observed. The percentage of ROS scavenging in NIH/3T3 cells was smaller than the one in AW264.7 cells, which could be attributed to the varied cellular uptake of MAC0.05@BSA to these two cell lines.

Following the *in vitro* assays of MAC0.05 in a monolayer cell model, a more complex cell system was utilised to evaluate

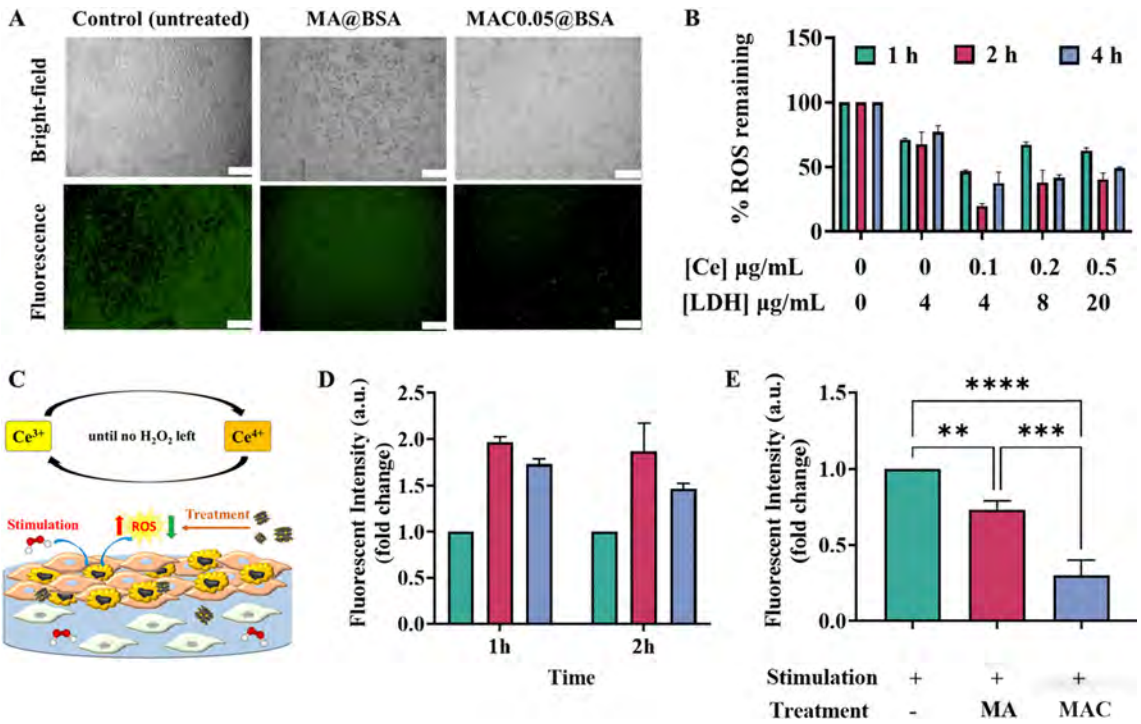

Fig. 5 *In vitro* ROS scavenging capability of MAC0.05@BSA in one-layered-cell and 3D-layered-cell constructs. (A) Bright-field and fluorescence images of RAW264.7 macrophages stained with DCFH-DA after stimulation and treatment by MA@BSA and MAC0.05@BSA. Scale bars: 100 μm. (B) Percentage of intracellular ROS after the treatment with MA@BSA ([Ce] = 0 μg mL^{-1} and [LDH] = 4 μg mL^{-1}) and different concentrations of MAC0.05@BSA after different incubation times in a monolayered cell model. The control group has [Ce] = 0 μg mL^{-1} and [LDH] = 0 μg mL^{-1}, simulated with H_2O_2. (C) Schematic illustration of stimulation and treatment by MAC0.05@BSA-mediated ROS scavenging in a 3D-layered-cell construct. (D) Cellular uptake of MA-FITC@BSA (red) and MAC0.05-FITC@BSA (blue) with the concentration of whole LDH (green control) at 4 μg mL^{-1}, incubated in 1 h and 2 h in a 3D cell-hydrogel system. (E) The ROS scavenging capability of MA@BSA and MAC0.05@BSA with the concentration of whole LDH at 4 μg mL^{-1}, incubated in 2 h, followed by ROS simulated with 1.5 mM of H_2O_2 in 30 min in a 3D cell-hydrogel system.

Ce–LDH NPs' effectiveness in anti-ROS. As shown in Fig. 5C, this system was constructed with three different cell lines that were combined to mimic a simple model of an inflammatory vessel. In this system, smooth muscle cells (MOVAS) were loaded into a hydrogel layer made with Rat Collagen type I, and then a second layer of endothelial cells (SVEC) was cultured onto the hydrogel, followed by the third layer of macrophages (RAW 264.7) topping up.

Fig. 5D shows the cellular uptake in the established 3D cell-hydrogel system. MAC0.05-FITC@BSA demonstrated a slightly lower uptake than MA-FITC@BSA. These data were consistent with the cellular uptake results when testing with the monolayered cell model. This lower uptake capability would be ascribed to the larger sizes of LDH NPs after loading with Ce, which reduced the cellular uptake of these NPs. On the other hand, even though it showed smaller percentages of cellular uptake, MAC0.05@BSA performed significant higher ROS scavenging capability than MA@BSA (Fig. 5E). After 2 h treatment, up to 70% of ROS was quenched compared to non-treated control group, corroborating the effectiveness of MAC0.05 as a potential treatment agent at inflammatory sites.

Conclusions

In summary, we reported the development of Ce–LDH nanoparticles (MAC) as the inorganic antioxidants for inflammation treatment through ROS scavenging. The MAC was prepared by incorporating Ce into LDHs by partially replacing Al^{3+} with Ce^{3+} in MgAl–LDH. Various Ce^{3+} percentages were tested, and physicochemical analyses confirmed the successful intercalation of Ce into LDH sheets while maintaining the characteristic properties of both nanoceria and LDH nanoparticles. The coprecipitation method preserved the structural integrity of the Ce–LDH NPs and endowed them with SOD mimetic activity through the regeneratable redox cycling between Ce^{3+} and Ce^{4+}. Through XPS and fluorescence analysis, the surface and bulk Ce^{3+}/Ce^{4+} ratios were determined, and a 5% Ce^{3+} substitution was optimal, making MAC0.05 the primary candidate for further ROS scavenging. *In vitro* test using CUPRAC method showed that MAC0.05 can quenching 64.8% of 0.4 mM H_2O_2, which is about 1.5 times higher than that of commonly used CeO_2 NPs. After functionalisation with FITC and BSA, MAC0.05 retained its stability in various solutions and showed enhanced ROS-scavenging efficiency. In a complex three-layered cell model, MAC0.05@BSA could scavenge up to 70% of ROS in stimulated macrophages. This study thus provides a new strategy for the development of LDH-based nano-antioxidant as the ROS-scavenging agent for potential applications in inflammatory disease treatment.

Conflicts of interest

There are no conflicts to declare.

Data availability

Data are available from the authors upon request.

Supplementary information available: Experimental details, additional characterisation data of MAC nanoparticles, and cell analyses. See DOI: **https://doi.org/10.1039/d5tb00829h**

Acknowledgements

This work was supported by Australian Research Council (ARC) Discovery Projects (DP190103486) and National Health and Medical Research Council (APP1175808, APP2002827). The author Thanh-Truc Nguyen wants to express their gratitude to the ''Vingroup Science and Technology Scholarship Program for Overseas Study for Master's and Doctoral Degrees'' for financially supporting their MPhil program at The University of Queensland. Hang Thu Ta was supported by a Heart Foundation Future Leader Fellowship (106521). Assistance of Australian Microscopy & Microanalysis Research Facility at the Centre for Microscopy and Microanalysis (CMM) and Queensland Node of the Australian National Fabrication Facility (ANFF-Q), the University of Queensland, are also acknowledged.

Notes and references

1 D. Furman, J. Campisi, E. Verdin, P. Carrera-Bastos, S. Targ, C. Franceschi, L. Ferrucci, D. W. Gilroy, A. Fasano, G. W. Miller, A. H. Miller, A. Mantovani, C. M. Weyand, N. Barzilai, J. J. Goronzy, T. A. Rando, R. B. Effros, A. Lucia, N. Kleinstreuer and G. M. Slavich, *Nat. Med.*, 2019, **25**, 1822–1832.
2 P. H. Black, *Brain, Behav., Immun.*, 2002, **16**, 622–653.
3 R. Strawbridge, D. Arnone, A. Danese, A. Papadopoulos, A. Herane Vives and A. J. Cleare, *Eur. Neuropsychopharmacol.*, 2015, **25**, 1532–1543.
4 S. C. Pike, M. Havrda, F. Gilli, Z. Zhang and L. A. Salas, *npj Parkinson's Dis.*, 2024, **10**, 21.
5 A. F. Mendes, M. T. Cruz and O. Gualillo, *Front. Physiol.*, 2018, **9**, 1741.
6 F. Zhang, A. H. Jonsson, A. Nathan, N. Millard, M. Curtis, Q. Xiao, M. Gutierrez-Arcelus, W. Apruzzese, G. F. M. Watts, D. Weisenfeld, S. Nayar, J. Rangel-Moreno, N. Meednu, K. E. Marks, I. Mantel, J. B. Kang, L. Rumker, J. Mears, K. Slowikowski, K. Weinand, D. E. Orange, L. Geraldino-Pardilla, K. D. Deane, D. Tabechian, A. Ceponis, G. S. Firestein, M. Maybury, I. Sahbudin, A. Ben-Artzi, A. M. Mandelin, A. Nerviani, M. J. Lewis, F. Rivellese, C. Pitzalis, L. B. Hughes, D. Horowitz, E. DiCarlo, E. M. Gravallese, B. F. Boyce, J. Albrecht, J. L. Barnas, J. M. Bathon, D. L. Boyle, S. L. Bridges, D. Campbell, H. L. Carr, A. Chicoine, A. Cordle, P. Dunn, L. Forbess, P. K. Gregersen, J. M. Guthridge, L. B. Ivashkiv, K. Ishigaki, J. A. James, G. Keras, I. Korsunsky, A. Lakhanpal, J. A. Lederer, Z. J. Li, Y. Li, A. McDavid, M. J. McGeachy, K. Raza, Y. Reshef, C. Ritchlin, W. H. Robinson, S. Sakaue, J. A. Seifert, A. Singaraju, M. H. Smith, D. Scheel-Toellner, P. J. Utz, M. H. Weisman, A. Wyse, Z. Zhu, L. W. Moreland, S. M. Goodman, H. Perlman,

V. M. Holers, K. P. Liao, A. Filer, V. P. Bykerk, K. Wei, D. A. Rao, L. T. Donlin, J. H. Anolik, M. B. Brenner, S. Raychaudhuri and R. A. S. L. E. N. Accelerating Medicines Partnership, *Nature*, 2023, **623**, 616–624.
7 J.-H. Han, R. Karki, R. K. S. Malireddi, R. Mall, R. Sarkar, B. R. Sharma, J. Klein, H. Berns, H. Pisharath, S. M. Pruett-Miller, S.-J. Bae and T.-D. Kanneganti, *Nat. Commun.*, 2024, **15**, 1739.
8 M. P. Murphy and L. A. J. O'Neill, *Nature*, 2024, **626**, 271–279.
9 N. Xiao, M. Nie, H. Pang, B. Wang, J. Hu, X. Meng, K. Li, X. Ran, Q. Long, H. Deng, N. Chen, S. Li, N. Tang, A. Huang and Z. Hu, *Nat. Commun.*, 2021, **12**, 1618.
10 D. Arsenijevic, H. Onuma, C. Pecqueur, S. Raimbault, B. S. Manning, B. Miroux, E. Couplan, M.-C. Alves-Guerra, M. Goubern, R. Surwit, F. Bouillaud, D. Richard, S. Collins and D. Ricquier, *Nat. Genet.*, 2000, **26**, 435–439.
11 J. Liu, M. Wu, R. Zhang and Z. P. Xu, *View*, 2021, **2**, 20200139.
12 C. Martinelli, C. Pucci, M. Battaglini, A. Marino and G. Ciofani, *Adv. Healthcare Mater.*, 2020, **9**, 1901589.
13 J. Liu, X. Han, T. Zhang, K. Tian, Z. Li and F. Luo, *J. Hematol. Oncol.*, 2023, **16**, 116.
14 X. Huang, D. He, Z. Pan, G. Luo and J. Deng, *Mater. Today Bio*, 2021, **11**, 100124.
15 J. Zhang, Y. Fu, P. Yang, X. Liu, Y. Li and Z. Gu, *Adv. Mater. Interfaces*, 2020, **7**, 2000632.
16 Y. E. Kim and J. Kim, *ACS Appl. Mater. Interfaces*, 2022, **14**, 23002–23021.
17 S. Tiwari, *Reactive Oxygen Species in Plants*, 2017, pp. 187–203, DOI: **10.1002/9781119324928.ch10**.
18 S. Mukherjee, V. S. Madamsetty, D. Bhattacharya, S. Roy Chowdhury, M. K. Paul and A. Mukherjee, *Adv. Funct. Mater.*, 2020, **30**, 2003054.
19 E. Hood, E. Simone, P. Wattamwar, T. Dziubla and V. Muzykantov, *Nanomedicine*, 2011, **6**, 1257–1272.
20 Y. Zhu, R. Shi, W. Lu, S. Shi and Y. Chen, *Nanoscale*, 2024, **16**, 7363–7377.
21 B. Zhu, J. Wu, T. Li, S. Liu, J. Guo, Y. Yu, X. Qiu, Y. Zhao, H. Peng, J. Zhang, L. Miao and H. Wei, *Adv. Healthcare Mater.*, 2024, **13**, 2302485.
22 S. Das, J. M. Dowding, K. E. Klump, J. F. McGinnis, W. Self and S. Seal, *Nanomedicine*, 2013, **8**, 1483–1508.
23 A. Dhall and W. Self, *Antioxidants*, 2018, **7**, 97.
24 Y. Wu and H. T. Ta, *J. Mater. Chem. B*, 2021, **9**, 7291–7301.
25 Y. Wu, Y. Yang, W. Zhao, Z. P. Xu, P. J. Little, A. K. Whittaker, R. Zhang and H. T. Ta, *J. Mater. Chem. B*, 2018, **6**, 4937–4951.
26 G. Varga, T.-T. Nguyen, J. Wang, D. Tian, R. Zhang, L. Li and Z. P. Xu, *ACS Appl. Mater. Interfaces*, 2024, **16**, 11453–11466.
27 T. Ye, W. Huang, L. Zeng, M. Li and J. Shi, *Appl. Catal., B*, 2017, **210**, 141–148.
28 Y. Wu, K. X. Vazquez-Prada, Y. Liu, A. K. Whittaker, R. Zhang and H. T. Ta, *Nanotheranostics*, 2021, **5**, 499–514.
29 M. F. Montemor, A. M. Simões, M. G. S. Ferreira and M. J. Carmezim, *Appl. Surf. Sci.*, 2008, **254**, 1806–1814.
30 B. A. Rzigalinski, C. S. Carfagna and M. Ehrich, *Wiley Interdiscip. Rev.: Nanomed. Nanobiotechnol.*, 2017, **9**, e1444.
31 D. E. L. Vieira, A. N. Salak, M. G. S. Ferreira, J. M. Vieira and C. M. A. Brett, *Appl. Surf. Sci.*, 2022, **573**, 151527.
32 V. K. Ameena Shirin, R. Sankar, A. P. Johnson, H. V. Gangadharappa and K. Pramod, *J. Controlled Release*, 2021, **330**, 398–426.
33 H. Xu, C. Shan, X. Wu, M. Sun, B. Huang, Y. Tang and C.-H. Yan, *Energy Environ. Sci.*, 2020, **13**, 2949–2956.
34 J. Liu, L. Li, R. Zhang and Z. P. Xu, *Nanoscale Horiz.*, 2023, **8**, 279–290.
35 G. Mishra, B. Dash and S. Pandey, *Appl. Clay Sci.*, 2018, **153**, 172–186.
36 Q. Wang and D. O'Hare, *Chem. Rev.*, 2012, **112**, 4124–4155.
37 P. Braterman, Z. P. Xu and F. Yarberry, *Layered Double Hydroxides*, 2004, 373–474.
38 W. Jin and D.-H. Park, *Nanomaterials*, 2019, **9**, 1404.
39 T. Hu, Z. Gu, G. R. Williams, M. Strimaite, J. Zha, Z. Zhou, X. Zhang, C. Tan and R. Liang, *Chem. Soc. Rev.*, 2022, **51**, 6126–6176.
40 W. Shen, T. Hu, X. Liu, J. Zha, F. Meng, Z. Wu, Z. Cui, Y. Yang, H. Li, Q. Zhang, L. Gu, R. Liang and C. Tan, *Nat. Commun.*, 2022, **13**, 3384.
41 T. Hu, W. Shen, F. Meng, S. Yang, S. Yu, H. Li, Q. Zhang, L. Gu, C. Tan and R. Liang, *Adv. Mater.*, 2023, **35**, 2209692.
42 Y. Yang, T. Hu, K. Zhao, Y.-C. Wang, Y. Zhu, S. Wang, Z. Zhou, L. Gu, C. Tan and R. Liang, *Adv. Mater.*, 2025, **37**, 2405847.
43 Y. Yang, T. Hu, Y. Bian, F. Meng, S. Yu, H. Li, Q. Zhang, L. Gu, X. Weng, C. Tan and R. Liang, *Adv. Mater.*, 2023, **35**, 2211205.
44 Z. Lv, T. Hu, Y. Bian, G. Wang, Z. Wu, H. Li, X. Liu, S. Yang, C. Tan, R. Liang and X. Weng, *Adv. Mater.*, 2023, **35**, 2206545.
45 V. Dev, N. Eigler, M. C. Fishbein, Y. Tian, A. Hickey, E. Rechavia, J. S. Forrester and F. Litvack, *Cathet. Cardiovasc. Diagn.*, 1997, **41**, 324–332.
46 S. Veeranarayanan, A. Cheruvathoor Poulose, S. Mohamed, A. Aravind, Y. Nagaoka, Y. Yoshida, T. Maekawa and D. S. Kumar, *J. Fluoresc.*, 2012, **22**, 537–548.
47 R. Apak, S. Gorinstein, V. Böhm, K. M. Schaich, M. Özyürek and K. Güçlü, *Pure Appl. Chem.*, 2013, **85**, 957–998.
48 J. Liu, Y. Wu, C. Fu, B. Li, L. Li, R. Zhang, T. Xu and Z. P. Xu, *Small*, 2020, **16**, 2002115.
49 Z. P. Xu and G. Q. Lu, *Chem. Mater.*, 2005, **17**, 1055–1062.
50 W. Xiao, Q. Guo and E. G. Wang, *Chem. Phys. Lett.*, 2003, **368**, 527–531.
51 R. Eloirdi, P. Cakir, F. Huber, A. Seibert, R. Konings and T. Gouder, *Appl. Surf. Sci.*, 2018, 457.
52 Y. A. Teterin, A. Y. Teterin, A. M. Lebedev and I. O. Utkin, *J. Electron Spectrosc. Relat. Phenom.*, 1998, **88–91**, 275–279.
53 I. A. Darwish, A. S. Khedr, H. F. Askal and R. M. Mahmoud, *Il Farmaco*, 2005, **60**, 555–562.
54 M. Alanazi, J. Yong, M. Wu, Z. Zhang, D. Tian and R. Zhang, *Chem. – Asian J.*, 2024, **19**, e202400105.
55 Z. Gu, H. Zuo, L. Li, A. Wu and Z. P. Xu, *J. Mater. Chem. B*, 2015, **3**, 3331–3339.
56 Y. Liu, Y. Wu, R. Zhang, J. Lam, J. C. Ng, Z. P. Xu, L. Li and H. T. Ta, *ACS Appl. Bio. Mater.*, 2019, **2**, 5930–5940.

Intercalating cerium into layered double hydroxide as a promising reactive oxygen species scavenger for inflammation treatment

Thanh-Truc Nguyen,[a] Gábor Varga,[a,d] Jessica Pickett,[b] Miaomiao Wu,[a] Hang T. Ta,[b]* Zhi Ping Xu,[a,c]* Run Zhang[a]*

[a] Australian Institute for Bioengineering and Nanotechnology, The University of Queensland, St Lucia, Queensland 4072, Australia

[b] School of Environment and Science, Griffith University, Nathan, Queensland 4111, Australia

[c] Institute of Biomedical Health Technology and Engineering and Institute of Systems and Physical Biology, Shenzhen Bay Laboratory, Shenzhen 518107, China

[d] Interdisciplinary Excellence Centre, Department of Applied and Environmental Chemistry, University of Szeged, Rerrich Béla tér 1, Szeged H-6720, Hungary

Corresponding authors

Prof Hang T. Ta, Email: h.ta@griffith.edu.au

Prof Zhi Ping Xu, Email: gordonxu@uq.edu.au

Dr Run Zhang, Email: r.zhang@uq.edu.au

Experimental section

Synthesis of cerium oxide (CeO_2) nanoparticles

The precursor nanoparticle solution was prepared by dissolving 0.685 g ceric ammonium nitrate $(NH_4)_2Ce(NO_3)_6$ and 2.5 g sodium acetate (CH_3COONa) in 17.5 mL DI water. After that, 2.5 mL of acetic acid (CH_3COOH) was added into the solution, and the mixture was stirred for 1 h at room temperature. Then, the mixture was left to incubate at 100°C for 3 h. The prepared nanoparticles were obtained after centrifugation at 6,000 g for 10 min and washing with 4 mL Milli-Q water. The pellet was resuspended in 4 mL of DI water for future use of anti-H_2O_2 capability test.

Synthesis of MAC LDH NPs with different percentages of Al^{3+} replaced by Ce^{3+} (Figure S1)

A coprecipitation protocol was used to synthesize $Mg_xAl_{1-y}Ce_y$ – LDH NPs (MAC) with x = 2.5 and y = 0 – 0.2. Specifically, a solution of 20 mL 0.75 M NaOH was added quickly to a mixture of 10 mL solution containing $MgCl_2•6H_2O$ (0.5 M), $AlCl_3•6H_2O$ (from 0.16 to 0.195 M), and $CeCl_3•7H_2O$ (from 0.005 to 0.04 M) under vigorous stirring and nitrogen (N_2) bubbling for the first 5 min. Then, the mixture was stirred at room temperature for another 1 h, and the slurry was collected after centrifugation (4,500 g) for 5 min. After washing with water for 3 times, the produced LDH NPs were suspended in Milli-Q water for stabilisation for 5 days before undergone any dilution for further experiments. The different percentages of aluminium replaced by cerium were 0%, 2.5%, 5%, 10%, 15%, and 20%, which had the related samples be named as MA, MAC0.025, MAC0.05, MAC0.1, MAC0.15, and MAC0.2, respectively.

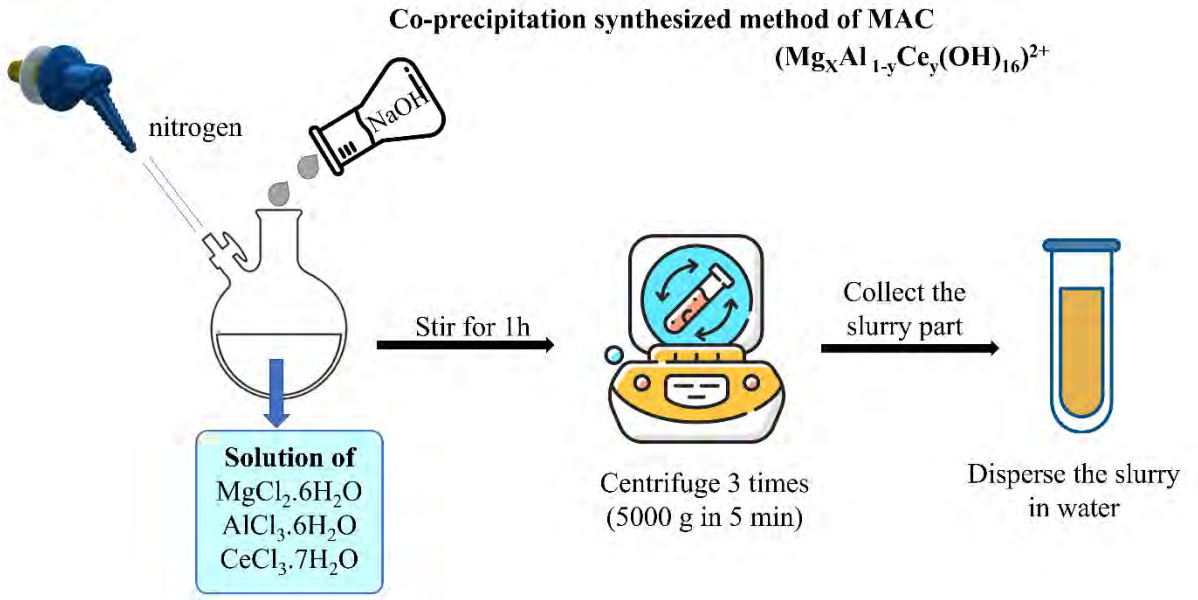

Figure S1. Schematic illustration of the synthesis procedure for preparation of MAC.

Labelling MAC0.05 with FITC and Coating BSA for *in vitro* experiments (Figure S2)

Labelling MAC0.05 with FITC

To label MAC0.05 with FITC, 1 mL of MAC0.05 1 mg/mL was mixed with 0.05 mL FITC (1 mg/mL in ethanol absolute 98%), then it was stirred at room temperature in the dark for 30 min. The slurry was centrifugation (4,500 g in 10 min) to remove the excess FITC. The final product (MAC0.05-FITC) is dispersed in Milli-Q water for further use.

Coating MAC0.05-FITC with BSA

MAC0.05-FITC was added slowly into a BSA solution under stirring for at least 30 min with the mass ratio of LDH:BSA = 1:5. The final product MAC0.05-FITC@BSA is dispersed in Milli-Q water for cellular uptake tests.

Coating MAC0.05 with BSA

MAC0.05 with different concentrations (1, 0.5, and 0.1 mg/mL) was added dropwise with a speed of 100 µL/min into a BSA solution with the mass ratio of LDH: BSA = 1:5, stirring for 30 min. The final product (MAC0.05@BSA) is dispersed in Milli-Q water for MTT assay, and colloidal stability in PBS and culture media, and ROS scavenging experiments. For colloidal

stability, 500 µL of MAC0.05@BSA was mixed with 500 µL of 1× PBS or culture media, and the size changes of MAC0.05@BSA were measured by Zetasizer Analyzer.

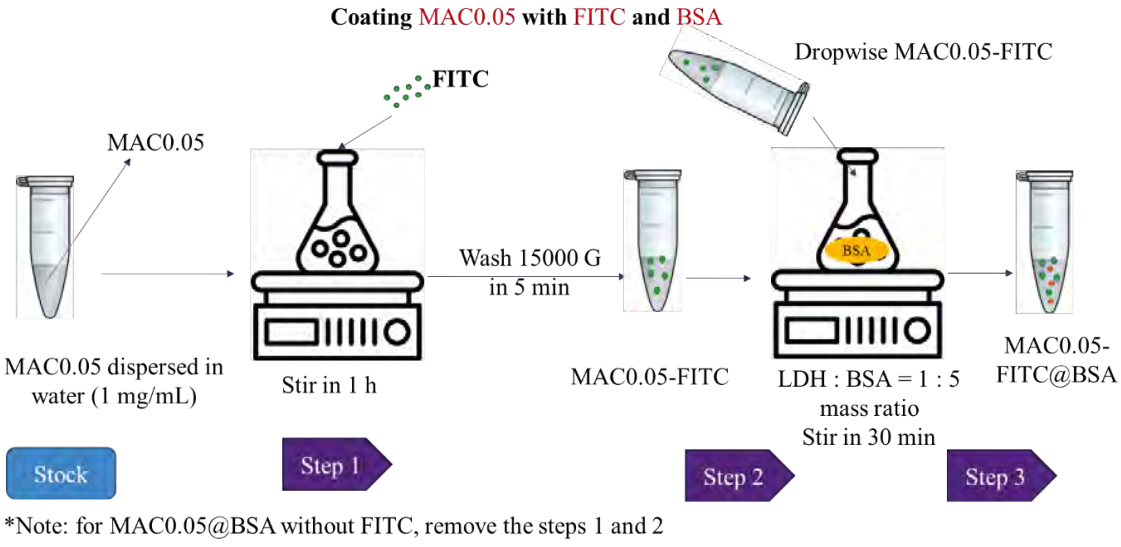

Figure S2. Schematic illustration of the procedure for labelling of MAC with FITC and coating with BSA.

Cellular uptake

Macrophages RAW 264.7 were seeded into a 24-well plate at a density of 25,000 cells per well and incubated for 24 h. The cell culture media was replaced with the new media containing MA-FITC@BSA and MAC0.05-FITC@BSA, both at the concentrations of 4 µg/mL and 20 µg/mL. After 24 h of incubation, the media was removed, and the fluorescence of suspended cells in 1× PBS in were analysed by flow cytometry ($\lambda_{ex/em}$ = 485/530 nm).

Cell viability

Macrophages RAW 264.7, A549, and NIH/3T3 cells were seeded into 96-well plates at a density of 5000 cells per well using DMEM High Glucose (10% FBS, 5% PS). After 24 h incubation, the cell culture media was replaced with the new media containing MA@BSA (at the concentration of 4 µg/mL) and MAC0.05@BSA (at the concentration of 4, 8, 20, and 40 µg/mL). The cells were then incubated for 24 h before treatment with 100 µL of MTT (0.5 mg/mL) for 4 h. The media containing excess MTT was removed. Then, 100 µL of DMSO was

added to each well. The absorbance was then measured in a Multimode Plate Reader within 30 min of DMSO addition. The absorbance of the control well which was treated with culture media only is regarded as 100% viability of the macrophages. The background well contained 100 µL of MTT (0.5 mg/mL) diluted with DMEM (10% FBS, 5% PS).

Statistical analysis of data

Data are presented as mean ± standard deviation (SD). One-way and two-way ANOVA were used in the analysis of significant differences. A p-value of ≤ 0.05 was considered significant.

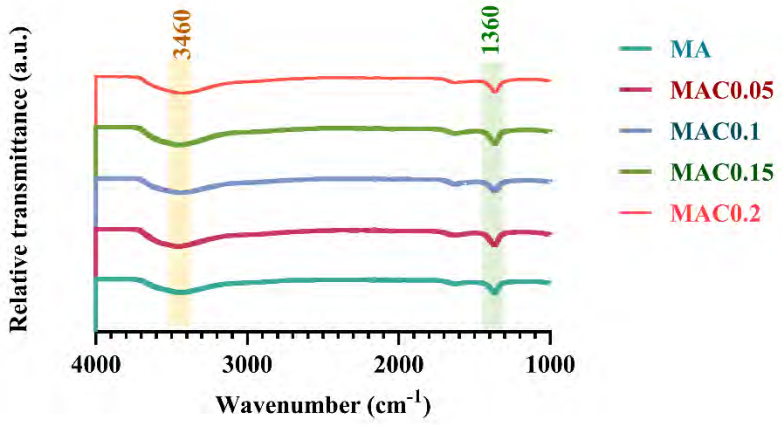

Figure S3. The FT-IR spectra of MA, MAC0.05, MAC0.1, MAC0.15, and MAC0.2.

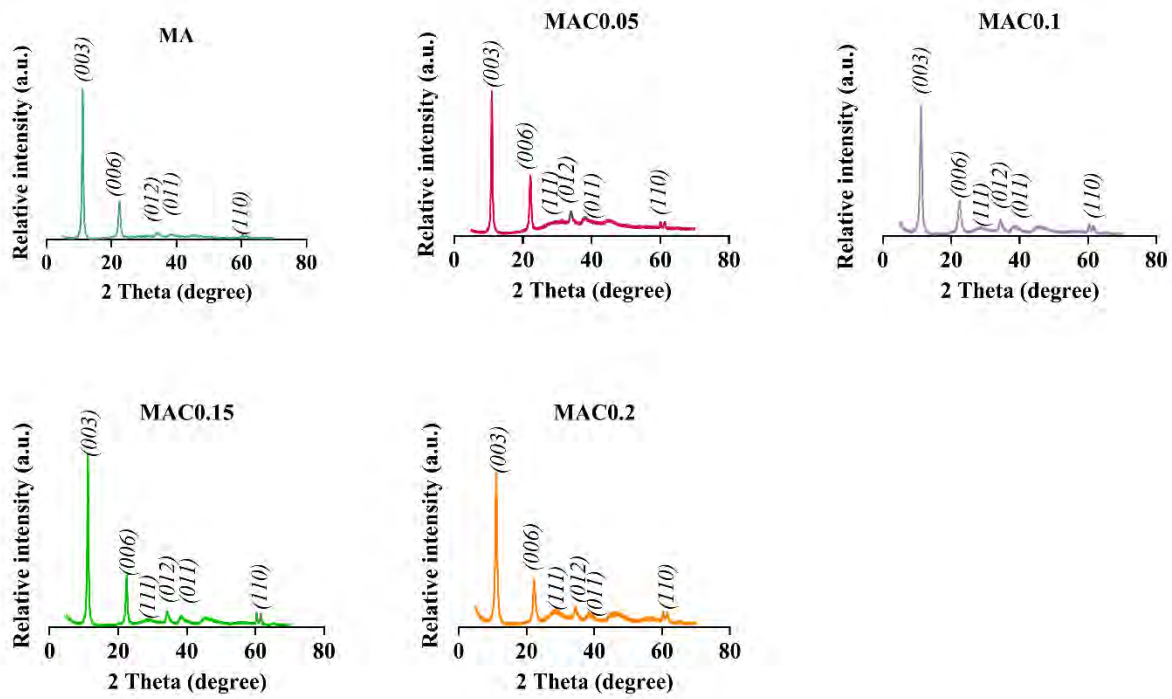

Figure S4. The XRD spectra of (A) MA, (B) MAC0.05, (C) MAC0.1, (D) MAC0.15, and (E) MAC0.2.

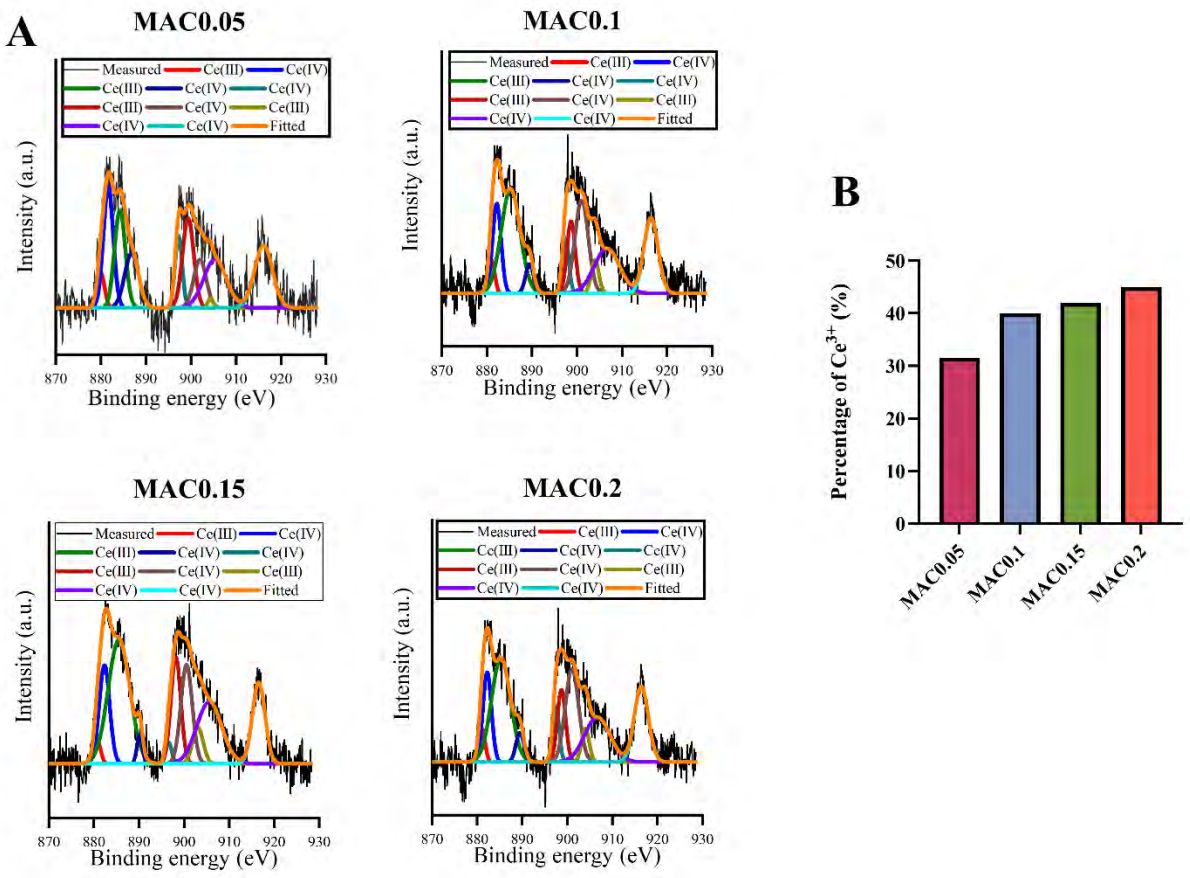

Figure S5. XPS spectra of (i) MAC0.05, (ii) MAC0.1, (iii) MAC0.15, (iv) MAC0.2, and (v) the percentage of Ce^{3+} in the surface of LDH calculated from XPS spectra.

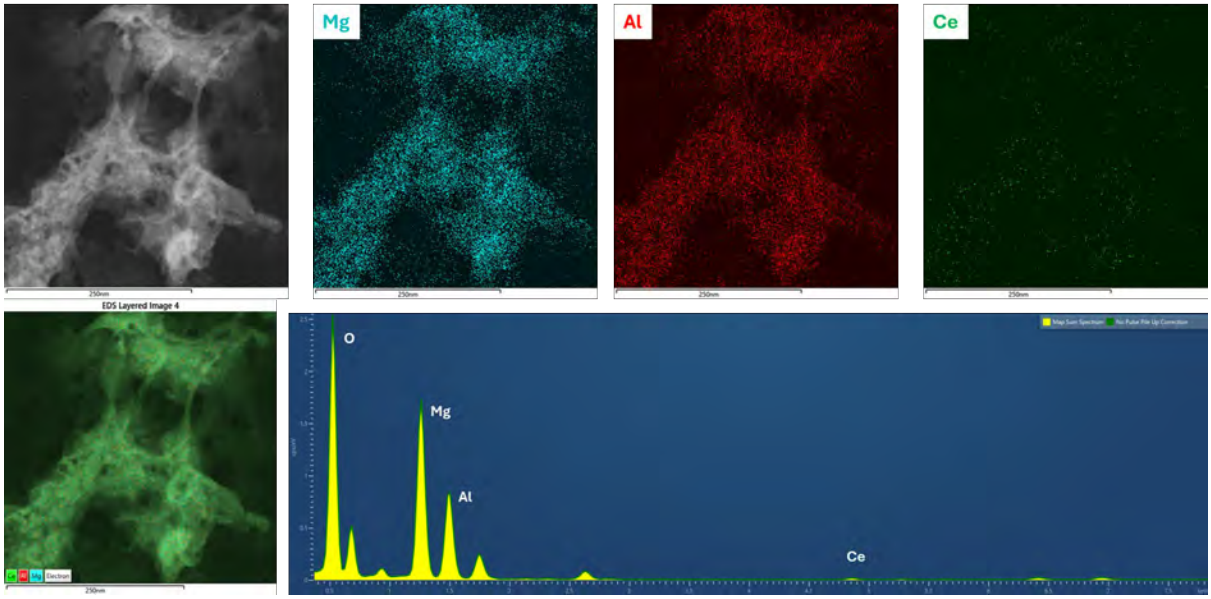

Figure S6. Elemental mapping and the EDX spectrum of MAC0.05.

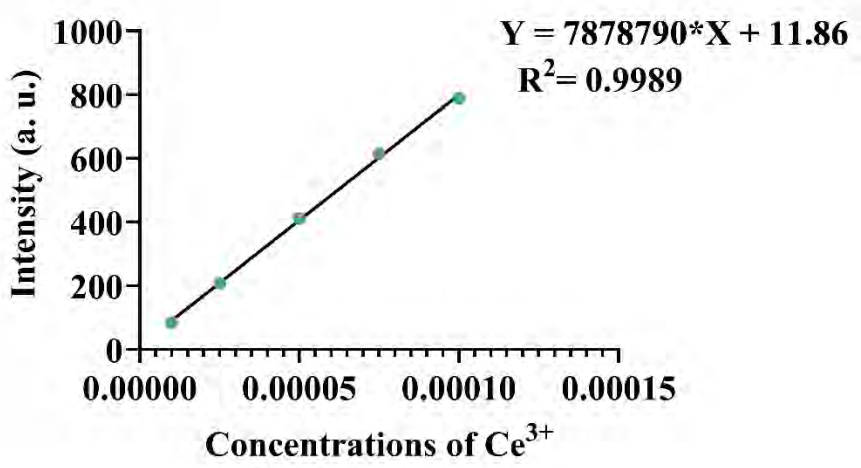

Figure S7. The standard curve of the experiment to calculate the percentage of Ce^{3+} in the bulk LDH using fluorometric method.

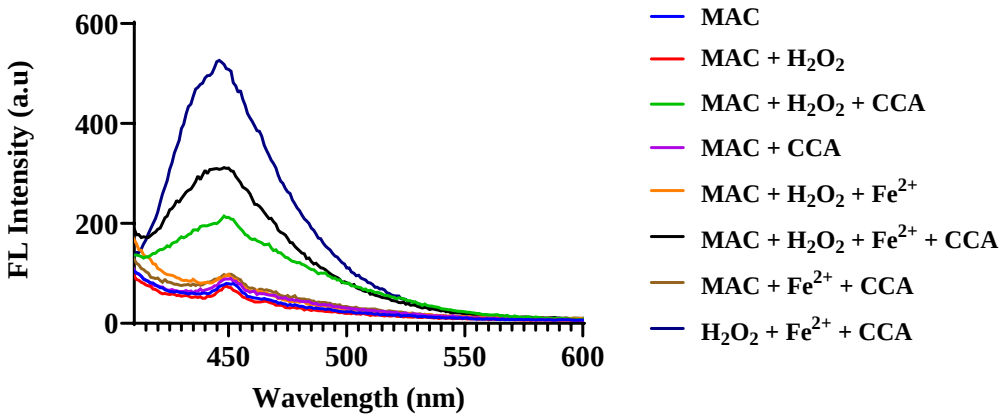

Figure S8. Fluorescence analysis of •OH in various systems using CCA as the probe.

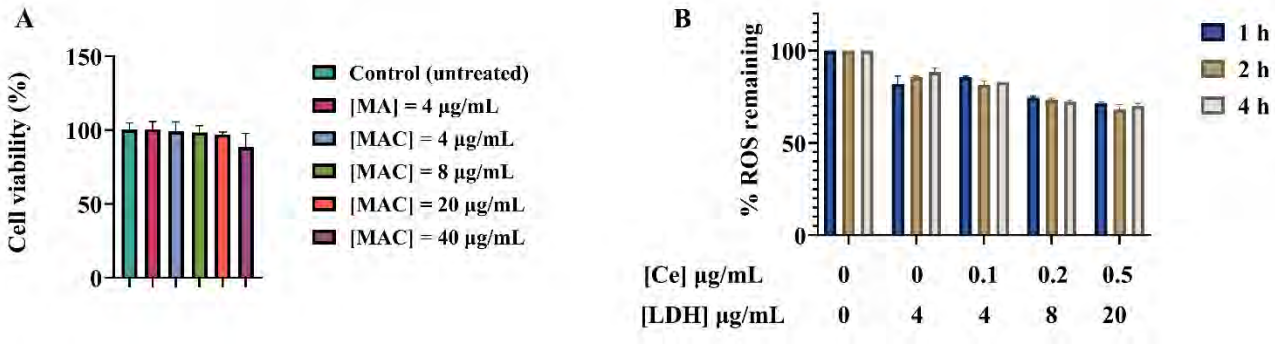

Figure S9. Cell analyses of MAC0.05@BSA to fibroblast NIH/3TC. (A) MTT cell viability assay of MAC0.05@BSA (0, 4, 8, 20, and 40 µg/mL) to fibroblast NIH/3TC. (B) ROS scavenging capability of MAC0.05@BSA (0, 4, 8, and 20 µg/mL) to H_2O_2 stimulated fibroblast NIH/3TC.

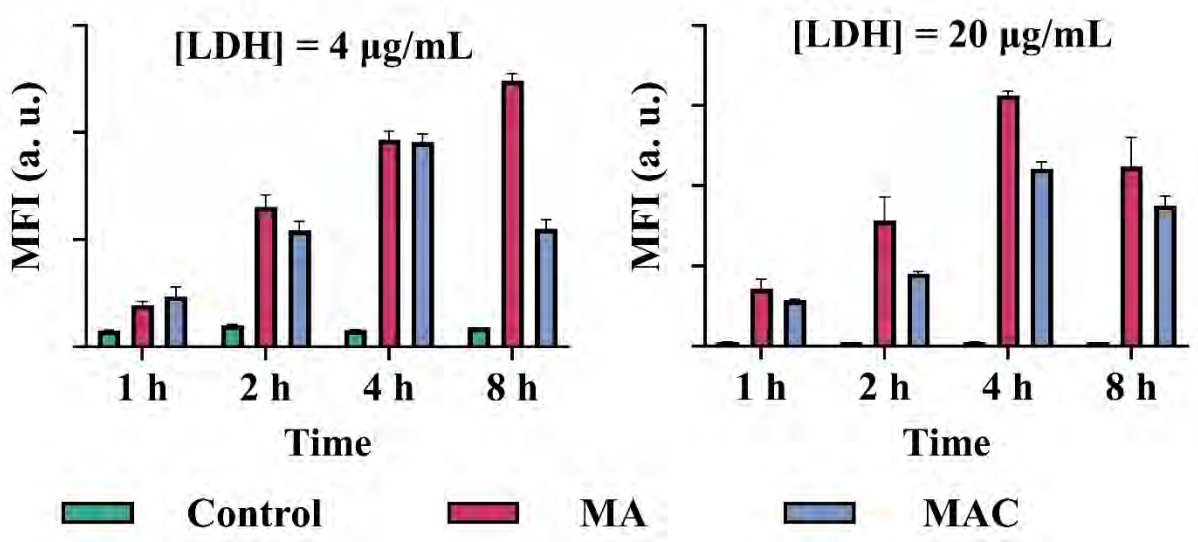

Figure S10. Cell uptake of MAC0.05@BSA in one-layered-cell construct (RAW264.7). The MFI obtained from flow cytometry tested with the concentrations of both MA-FITC@BSA and MAC0.05-FITC@BSA at (left) 4 µg/mL and (right) 20 µg/mL.